Anisotropic reflection of UV radiation at the top of the atmosphere: Characteristics and models obtained from Meteor 3/TOMS

Ciren Pubu and Zhanqing Li

Canada Centre for Remote Sensing, Ottawa, Ontario

Abstract. Reflection of solar radiation usually exhibits a strong dependence on viewing geometry relative to the Sun's position. Such a dependence needs taking into account in remote sensing studies employing satellite measurements made with scanning radiometers. While many investigations have been conducted concerning the angular variation of radiation in the total solar, visible, and IR wavelengths, no study was devoted to the UV radiation whose dependence on viewing geometry may differ from radiation in other spectral regions. On the basis of two and half years of Meteor-3/TOMS data (from January 1992 to May 1994) the angular characteristics of UV radiation reflected at the top of the atmosphere (TOA) were studied extensively. A set of angular dependence models (ADMs) was developed for UV radiation at 340, 360, and 380 nm over 10 scene types. The results show that the angular dependence of UV-reflected radiation is strong and rather different from that for total shortwave (SW) radiation as derived for the Earth Radiation Budget Experiment (ERBE). The largest discrepancy occurs under clear conditions over oceans for overhead Sun and large viewing zenith angles. The discrepancy in TOA mean albedos derived using the two sets of ADM can reach up to 48%. The discrepancy diminishes to about 10% for clear land scenes. Comparisons were also made for regional monthly mean TOA albedos over the whole globe derived from the ERBE SW ADM, TOMS UV ADM, and the assumption of isotropic reflection from an independent data set acquired by Nimbus 7/TOMS in January and July 1991. The differences exhibit an apparent zonal trend, large at high latitudes, moderate at midlatitudes, and small in the tropics.

1. Introduction

Remote sensing of the atmosphere-terrestrial system relies primarily on satellite observations made from specific Sun-target-sensor geometry with scanning radiometers. However, since most targets in the Earth-atmosphere system reflect light anisotropically [*Kimes et al.*, 1984; *Middleton et al.*, 1991], the magnitude of the observation depends not only on the target's inherent physical characteristics but also on the direction of the Sun and satellite with respect to the target [*Diner et al.*, 1999]. The dependence is thus often referred to as bidirectional reflectance distribution function (BRDF) or simply called angular dependence model (ADM). ADM is a set of anisotropic factors that can be used to convert radiance measurements made from a specific direction into radiant fluxes defined over the entire upper hemisphere. The angular conversion is essential to monitor the temporal evolution of a target using multiangle measurements [*Gutman*, 1991; *Wu et al.*, 1995] and to obtain top-of-atmosphere (TOA) [*Suttles et al.*, 1988; *Li et al.*, 1996] and surface albedos [*Li and Garand*, 1994] from satellite reflectance measurements. In addition, the characteristics of the angular dependence helps extract geophysical and biophysical parameters [*Privette et al.*, 1997; *Diner et al.*, 1999]. Therefore knowledge on the anisotropy of reflection by a target is crucial for remote sensing studies.

So far, many investigations have been conducted concerning the angular variations of total shortwave (SW) and visible radiation. Among the existing broadband TOA ADM, the Earth Radiation Budget Experiment (ERBE) ADM is the most comprehensive and complete one, which was constructed using data primarily from the Earth Radiation Budget (ERB) radiometer onboard Nimbus 7 [*Suttles*, 1988]. Various issues concerning the development and application of the broadband ADM was reviewed by *Li* [1996]. Note that the broadband ADM may not be applicable to narrowband observations, since the ADM is contingent upon the wavelength and spatial scale of the measurements under study [*Pinty and Verstraete*, 1992]. Specific ADM have been developed for visible and near-IR solar radiation as observed by AVHRR channels 1 and 2 [*Gutman*, 1989; *Cihlar et al.*, 1994; *Wu et al.* 1995; *Li et al.*, 1996], but so far, no ADM has been developed for UV radiation.

Concerns about a potential increase in the harmful UV radiation due to a steady decline in stratospheric ozone content stimulate the remote sensing of global surface UV dose rate [*Stolarski*, 1992]. Various methods have been proposed for retrieving surface UV flux from satellite [*Eck et al.*, 1995; *Lubin et al.*, 1998; *Li et al.*, 2000; *Herman et al.*, 1999; *Krotkov et al.*, 1999]. Most of the methods require UV hemispheric albedo at the TOA as a major input parameter denoting the attenuation of UV radiation due to scattering by clouds and aerosols. A lack of knowledge on the angular dependence of UV radiation impedes the accuracy of the retrieval. Often, ad hoc assumptions were made for the sake of conversion from reflected radiance to irradiance or from reflectance to albedo over an

Table 1. Number of Samples in Angular Bins Under Clear Over Land Conditions

	RAZ1	RAZ2	RAZ3	RAZ4	RAZ5	RAZ6	RAZ7	RAZ8
				$Cos\,\theta_0 = 0.9\text{--}1.0$				
VZA1	2641	5754	5941	6443	5897	5894	5714	2640
VZA2	1641	3593	3746	3067	3440	3972	3552	1662
VZA3	1796	3731	3748	3104	3186	4041	3559	1634
VZA4	1923	3812	3997	3602	2974	4057	3553	1669
VZA5	1854	4080	4253	3784	3917	4102	3644	1638
VZA6	413	954	936	790	865	1073	1102	564
				$Cos\,\theta_0 = 0.5\text{--}0.6$				
VZA1	2805	3822	4208	4600	4707	4430	3769	2625
VZA2	1938	2555	3014	2575	2593	3014	2534	1704
VZA3	2033	2559	3068	2644	2632	3195	2462	1608
VZA4	1702	2119	3080	2772	2531	3083	2381	1500
VZA5	842	1253	2570	2551	2541	2959	2147	1216
VZA6	84	191	470	567	620	648	547	368
				$Cos\,\theta_0 = 0.2\text{--}0.3$				
VZA1	254	864	1333	1037	727	2162	1788	582
VZA2	167	673	832	196	196	1618	1675	335
VZA3	139	573	663	211	202	1764	2022	545
VZA4	115	382	474	277	249	1714	2183	904
VZA5	120	163	218	239	356	1673	1944	1153
VZA6	60	113	117	110	121	299	377	510

The ranges of angles for each of the angular bins are defined as the same as in ERBE ADM [Li, 1996].

UV band. For example, Eck et al. [1995] assumed that the TOMS-measured bidirectional reflectivity is isotropic, and thus no angular correction was made in their retrieval. Model simulations of the UV radiative transfer indicates that the assumption may create errors in the retrieval of surface UV radiation by more than 20% at high latitudes [Krotkov et al., 1999]. As the first order of approximation, Wang et al. [2000] employed the ERBE SW ADM to convert TOMS-measured UV reflectance into albedo.

In light of the potential problems in acquiring TOA UV albedos, an attempt is made here to take advantage of the TOMS measurements made from a non-Sun-synchronous satellite, Meteor 3, to study and develop a set of ADM for UV radiation at three wavelengths, 340, 360, and 380 nm. A scene identification technique different from ERBE ADM was adopted owing to the limited information provided by TOMS measurements. UV ADM was still developed for four cloud classes over three common surface types, namely, clear over ocean, clear over land, clear over land-ocean mix, partly cloudy over ocean, partly cloudy over land, partly cloudy over land-ocean mix, mostly cloudy over ocean, mostly cloudy over land, mostly cloudy over land-ocean mix, and overcast. In this paper, discussion pertains mainly to three distinct sets of ADM for clear over ocean, clear over land, and overcast scenes. However, ADMs for partly cloudy and mostly cloudy scenes are also shown, since most of the pixels may fall into either of these two categories because of the coarse resolution of TOMS measurements. On the basis of the ADM developed here, uncertainties associate with the assumptions of isotropic reflection and that the UV ADM is the same as the ERBE SW ADM are evaluated. To help understand the characteristics of the UV ADM and their discrepancies with other ADM, radiative transfer modelling was carried out. Finally, regional monthly mean UV TOA albedos over the whole globe were calculated from Nimbus-7/TOMS measurements for January and July 1991 using three different sets of ADM. Their differences are discussed.

2. Data and Method

2.1. Meteor 3/TOMS

In the present study, derivation of the ADM for UV radiation is based on about two and half years (January 1992 to May 1994) of satellite observations made by the Total Ozone Mapping Spectrometer (TOMS) onboard the Meteor 3. TOMS is a cross-track scanning radiometer, which measures radiance backscattered by the atmosphere-surface system at six 1 nm ultraviolet bands. They include ozone-sensitive (centered around 305, 310, and 320 nm) and ozone-insensitive bands (centered around 340, 360, and 380 nm), respectively. Since the retrieval of surface UV radiation usually requires TOA albedo at ozone-insensitive regions with ozone as an input variable [Li et al., 2000], ADM is only derived for nonozone absorption bands, i.e., 340, 360, and 380 nm. In addition to measuring the reflected UV radiance, the TOMS aboard the Meteor 3 was also equipped with a rotating diffuser allowing simultaneous measurements of solar incident irradiance at the TOA. Therefore the effect of varying Earth-Sun distance and solar zenith angle are accounted for by calculating TOA reflectance. TOMS scanned the atmosphere-surface system in 3° steps up to 51° on each side of the nadir point (~60 by 60 km) in a direction perpendicular to the orbit plane. The maximum viewing zenith angle is 63.5°. The non-Sun-synchronous orbit of the Meteor 3 allows for observing the same target at different solar and viewing angles. Both the radiometric accuracy and the wavelength registration of TOMS measurements were assured through prelaunch and frequent onboard calibrations [Herman et al., 1996].

Spatially sampled level-2 TOMS data are used here to reduce the spatial coherence between consecutive cross scans that are largely overlapped by picking up one pixel and skipping every eight pixels [Li and Leighton, 1992]. Each sample represents approximately a 250 by 250 km region. The sampled data are then sorted into different angular bins in terms of
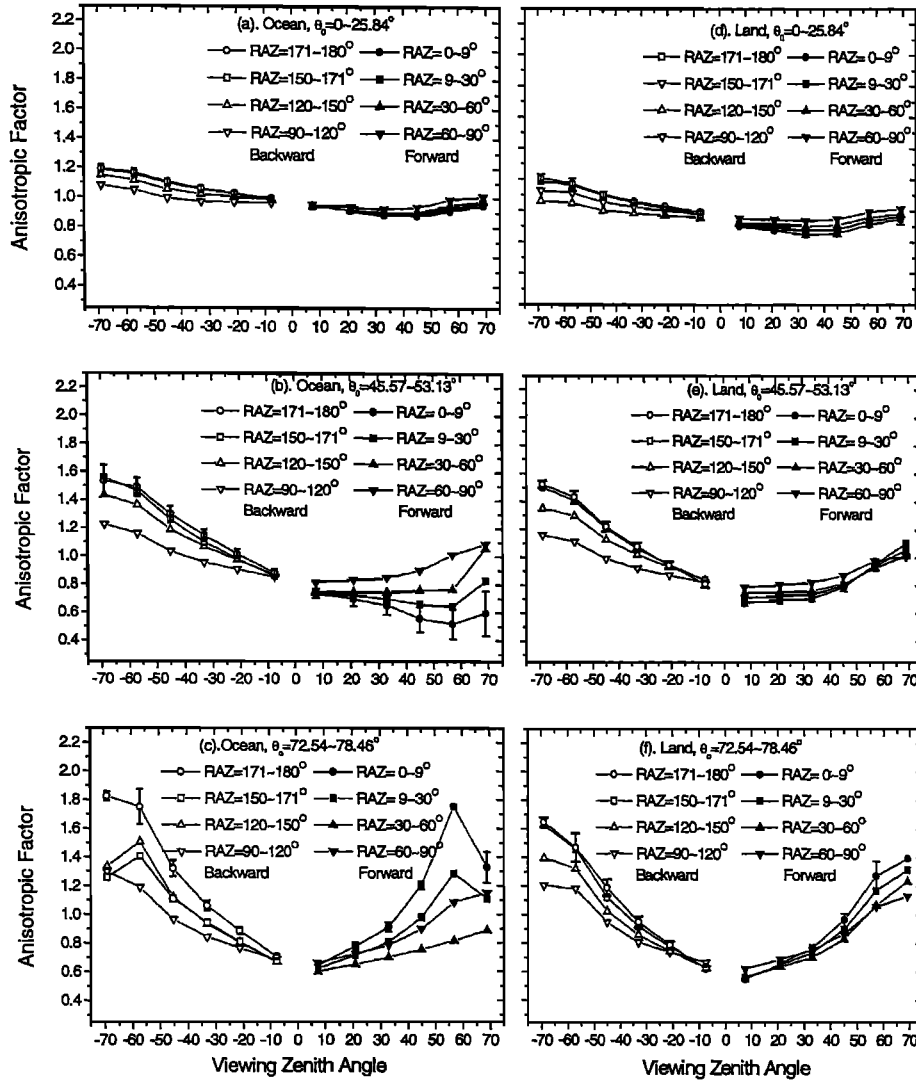
Figure 1. Anisotropic factor at 360 nm derived from Meteor-3 TOMS for clear over ocean and clear over land scenes. Note that positive (negative) viewing zenith angles represent forward (backward) directions.

solar zenith angle (SZA), viewing zenith angle (VZA), and relative azimuth angle (RAZ) between the Sun and the satellite, following the bin definition used in the ERBE ADM [*Suttles et al.*, 1988; *Li*, 1996]. A rough surface cover type for each pixel is included in the TOMS level-2 data as one of the following three categories: ocean, land, and land-ocean mix. Unlike the ERBE ADM which is based on the maximum-likelihood estimation technique, cloud amount is described by the effective cloud fraction (f) in this study; f is determined from a measured radiance at 380 nm ($I_{measured}$) [*Herman et al.*, 1996]:

$$f = \frac{I_{measured} - I_{ground}}{I_{cloud} - I_{ground}}, \qquad (1)$$

where I_{ground} is a model-calculated 380 nm radiance at TOA for a clear atmosphere over a snow/ice free ground with a reflectivity of 0.08. Surface pressure as a function of terrain height from NOAA is used to determine Rayleigh scattering for computing I_{ground}. If snow/ice is present, surface reflectivity is changed to 0.5. I_{cloud} is a modeled TOA radiance for an atmosphere containing a cloud layer with a reflectivity of 0.8.

Cloud top pressure derived from the International Satellite Cloud Climatology Project (ISCCP) was also used to compute I_{cloud}. The classification of cloud cover based on f is somewhat similar to the definition of cloud categories used in the ERBE ADM [*Suttles et al.*, 1988], namely, clear with $f < 5\%$, partly cloudy $5\% < f < 50\%$, mostly cloudy $50\% < f < 95\%$, and overcast $f > 95\%$. It must be stated, however, that the actual results of classification obtained by ERBE and here are not equivalent, since the former classifies a scene following the maximum-likelihood estimation (MLE) on the basis of prior statistics concerning shortwave and longwave flux measurements. Such statistics are not applicable to TOMS data due to the difference in their spectral coverage. Discrepancies in cloud scene identification could be attributed to differences in the ADM. Unfortunately, we cannot quantify these differences. It is assumed that the classification inconsistency is minimal for relatively pure scenes, namely, clear and overcast, which are addressed in more details in this paper. The overall probabilities of occurrence for clear, partly, mostly, and overcast scenes are 10-15%, 40-50%, 20-30%, and 5%, respectively.
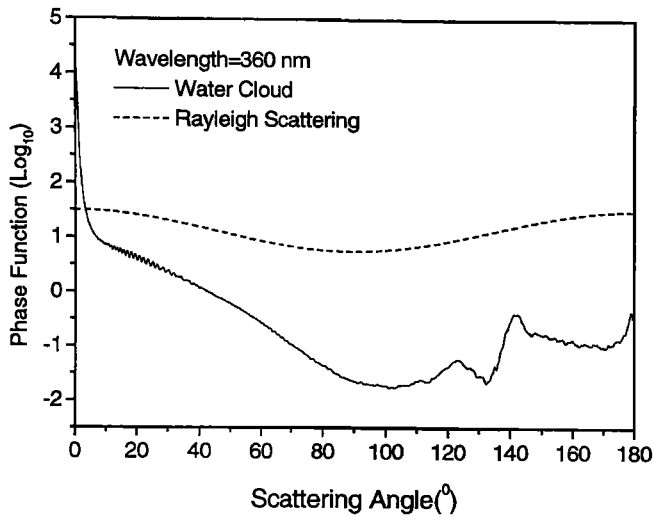
Figure 2. Phase functions of water clouds and Rayleigh scattering at 360 nm versus scattering angle.

While TOMS observations cover a large portion of the hemispheric domain, the number of samples in the angular bins distribute rather nonuniformly, ranging from tens of thousands to a few hundreds, as can be seen for a clear land scene (Table 1). There are fewer number of samples at large SZA and VZA and small RAZ. Fortunately, these bins contribute much less to the albedo due to a cosine response.

2.2. Angular Dependence Model

Following the definition of ADM for ERBE [*Suttles et al.*, 1988], an ADM, $R(\theta, \theta_0, \phi)$, is given as a function of SZA (θ_0), VZA (θ), and RAZ (ϕ):

$$R(\theta, \theta_0, \phi) = \frac{\pi L(\theta, \theta_0, \phi)}{M(\theta_0)}, \qquad (2)$$

where L represents a radiance measurement made from a specific Sun-target-satellite geometry. M denotes a radiative flux, which is only a function of SZA (θ_0). It can be calculated as

$$M(\theta_0) = \int_0^{2\pi} d\phi \int_0^{\pi/2} L(\theta, \theta_0, \phi) \cos\theta \sin\theta \, d\theta. \qquad (3)$$

TOA reflectance (a) and albedo (A) are described respectively as

$$a(\theta, \theta_0, \phi) = \frac{\pi L(\theta, \theta_0, \phi)}{F(\theta_0)}, \qquad (4)$$

$$A(\theta_0) = \frac{M(\theta_0)}{F(\theta_0)}, \qquad (5)$$

where F denotes the extraterrestrial solar flux incident on a horizontal surface at the TOA, which is also measured by TOMS. Combining (4) and (5), ADM can be further defined as

$$R(\theta, \theta_0, \phi) = \frac{a(\theta, \theta_0, \phi)}{A(\theta_0)}. \qquad (6)$$

It is clear that ADM can be determined if both reflectance and albedo are known. In this study, reflectance data are avail-

able from Meteor-3/TOMS level-2 data set, and albedo is calculated by

$$A(\theta_0) = \frac{1}{\pi} \int_0^{2\pi} d\phi \int_0^{\pi/2} a(\theta, \theta_0, \phi) \cos\theta \sin\theta \, d\theta. \qquad (7)$$

The integral in (7) is calculated by a numerical integration [*Suttle et al.*, 1988]:

$$\sum_{k=1}^{K} (\phi_{k+1} - \phi_k) \sum_{j=1}^{J} a_{jk}(\sin^2\theta_{j+1} - \sin^2\theta_j), \qquad (8)$$
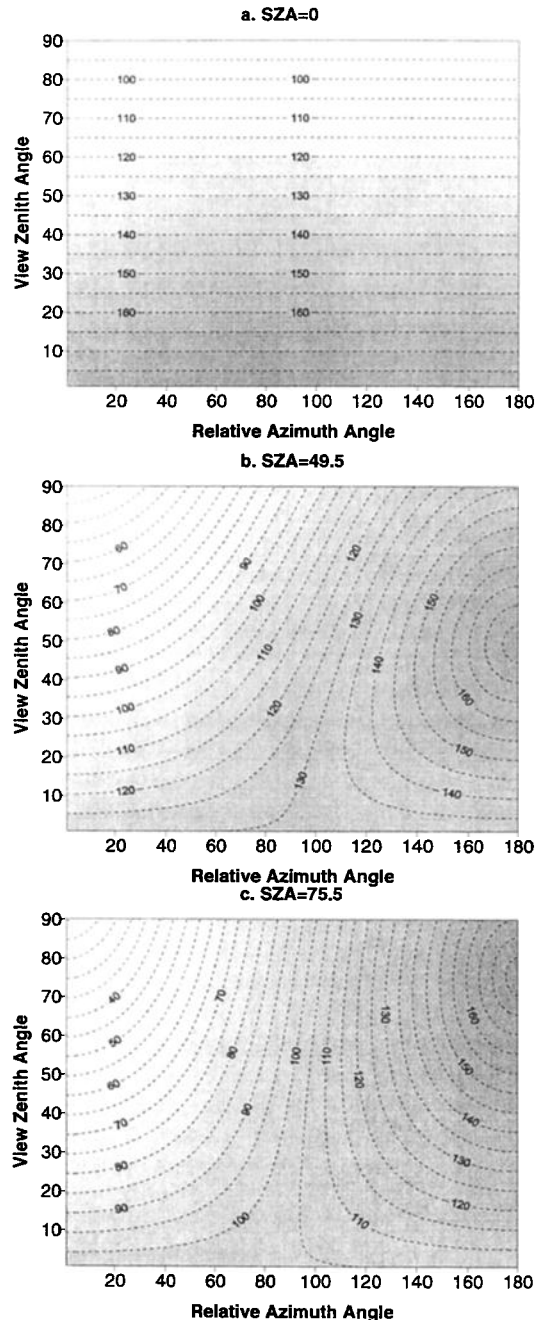

Figure 3. Variations of scattering angle with the viewing zenith angle (VZA) and relative azimuth angle (RAZ) at a solar zenith angle (SZA) of (a) 0°, (b) 49.5°, and (c) 75.5°, respectively.

where K and J is, respectively, the total number of RAZ bins and that of VZA bins; a_{ijk} is the mean reflectance in each discrete angular bin. Note that there are some empty bins for the largest viewing zenith angle (VZA bin 7) due to the limited scan angle (the maximum VZA is 63.5° for Meteor 3/TOMS), as well as some questionable bins due to small sample populations. The bins with a sample size less than 100 are treated as missing bins. In the integration, values at these invalid bins are determined by bilinear intrapolation and extrapolation [*Suttles et al.*, 1988] along both the azimuth angle direction and the viewing zenith angle direction.

2.3. Radiative Transfer Modeling

Radiative transfer modeling is instrumental in understanding the behaviour of the UV ADM and the discrepancies between various types of ADM. On the other hand, the observed ADM may provide a means of validating a radiative
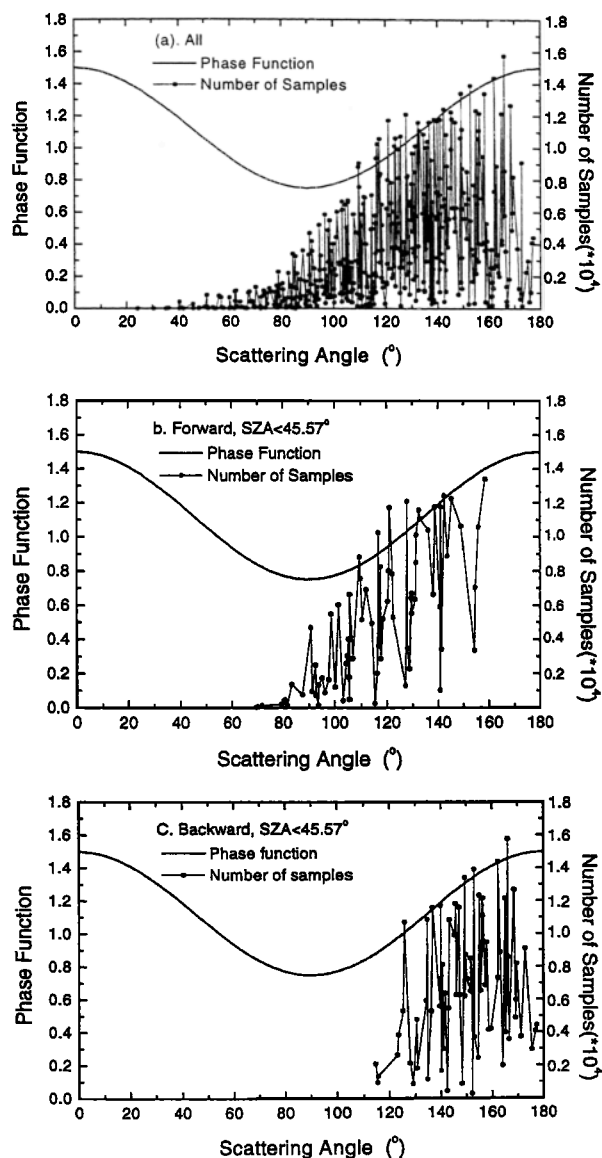
Figure 5. Simulated anisotropic factor at 360 nm for nearly overhead Sun with a surface albedo 0.0 and varying Rayleigh-scattering optical depth (τ_α).

transfer model. In these regards, radiative transfer simulations are conducted for both clear and cloudy conditions. The radiative transfer model used in this study is based on the discrete ordinate method, as described by *Stamnes et al.* [1988] and validated by *Tsay et al.* [1990]. The model includes all orders of multiple scattering and is valid for vertically inhomogeneous media. Under a plane parallel assumption the atmosphere is divided into a series of adjacent layers that are optically homogeneous but vary from one layer to another. Because of the curvature of the Earth the plane parallel assumption becomes invalid at a large solar zenith angle. Therefore a spherical version of the discrete ordinate model [*Dahlback et al.*, 1991] is applied when solar zenith angle becomes larger than 80°.

A clear atmosphere is divided into 34 layers. Atmospheric temperature and ozone profiles are based on the middle latitude summer atmosphere from LOWTRAN code [*Anderson et al.*, 1986]. A Lambertain surface is assumed. Ground-based measurements indicate that UV surface albedo is usually very small, less than 0.1 for the majority of the Earth's surface, except for snow-/ice-covered regions [*Weihs and Webb*, 1997]. Given that UV reflectivity is typically 0.02–0.04 over land and 0.05–0.08 over oceans [*Herman and Celarier*, 1997], the model simulations employ a surface albedo of 0.05. For simulation under a cloudy condition, a model cloud of Stratocumulus I defined by *Stephens* [1978] is inserted into the 1.5–2.5 km atmospheric layer. Since the single-scattering albedo is essentially equal to 1 and the asymmetry factor is very similar for various types of clouds in the UV band [*Pubu*, 1998], the radiative characteristics including the angular dependence for different types of water clouds are similar [*Fredrick and Snell*, 1990; *Fredrick and Weatherhead*, 1992].

Figure 4. Phase function of Rayleigh scattering at 360 nm, and the distribution of the number of samples with respect to scattering angle (a) for all samples and (b) for forward, and (c) for backward measurements when SZA is smaller than 45.57°.
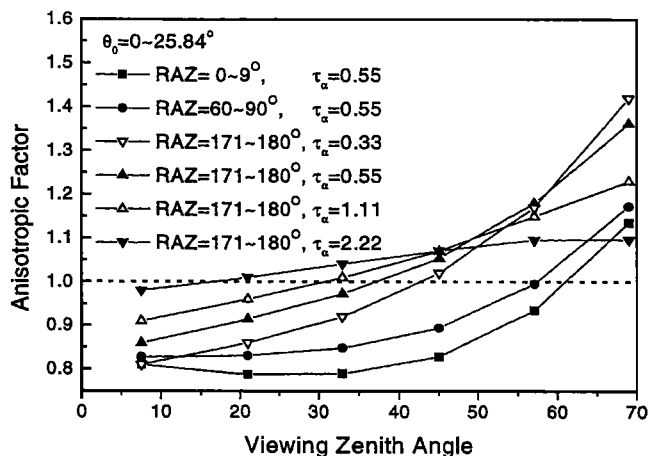
3. Results and Discussions

On the basis of two and half years of Meteor-3/TOMS data, ADM for UV radiation reflected at the TOA are derived at three wavelengths, 340, 360, and 380 nm over 10 different scene types. Only a handful of the ADM are presented and discussed here. All the ADM in tabulated format are available from the authors for general use.
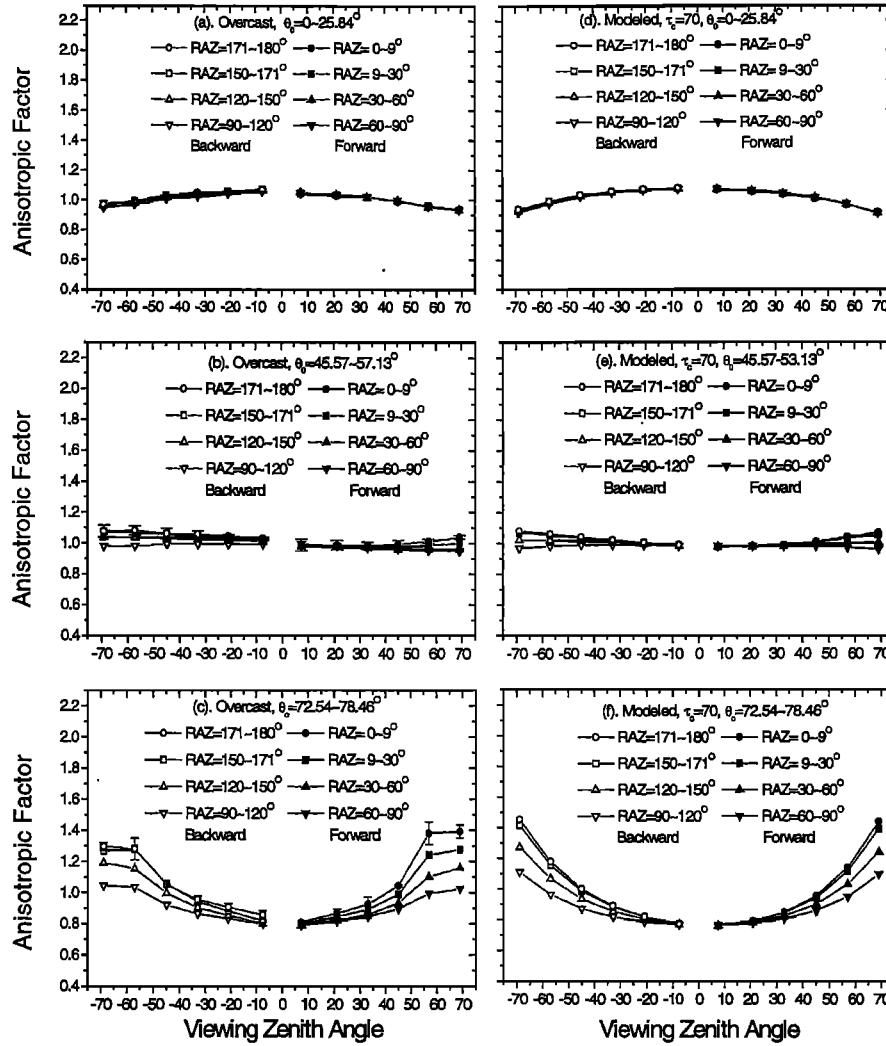
Figure 6. Anisotropic factor at 360 nm derived from Meteor-3 TOMS data in comparison with the simulated anisoptropic factor for an overcast atmosphere with a cloud optical depth (τ_c) of 70 at 550 nm. Rayleigh-scattering optical depth at 360 nm is 0.56.

3.1. Clear Ocean and Clear Land Scenes

Figure 1 shows the derived ADM at 360 nm for clear over ocean and clear over land scenes. It demonstrates that the reflection of UV radiation is highly anisotropic. In general, the UV radiation scattered in a backward direction is much stronger than in a forward direction, especially for low solar zenith angles. Yet, the reflection in backward directions appears to be more isotropic. As the SZA increases, scattering becomes more symmetric between the forward and the backward directions. For moderate and large SZAs (Figures 1b, 1c, 1e, and 1f) the variation of the anisotropic factor with RAZ is smaller for clear land scenes than for clear ocean scenes.

Note that the wavelengths of concern here are located in a strong Rayleigh scattering band. Since surface albedo for UV radiation is usually extremely small for snow-/ice-free surfaces [*Weihs and Webb*, 1997; *Herman et al.*, 1997], Rayleigh scattering is a major factor dictating the angular behavior of the UV radiation backscattered by the atmosphere under clear-sky conditions. Figure 2 shows the phase function of Rayleigh scattering whose strength varies drastically with the scattering angle (φ). It reaches maximum value at the very forward ($\varphi =$

$0°$) or backward ($\varphi = 180°$) scattering directions. The intensity of reflection is reduced to a little more than half of the peak value in the sideward scattering direction ($\varphi = 90°$). It is worth being emphasized that the "forward" and "backward," as marked in Figure 1, do not necessarily correspond to truly forward and backward scattering, as they were defined by the RAZ only, RAZ $< 90°$ being forward and RAZ $> 90°$ being backward. True backward or forward scattering is determined by the scattering angle that is determined by all three angles, namely SZA (θ_0), VZA (θ), and RAZ (ϕ). The true scattering angle (φ) is calculated by

$$\cos \varphi = \cos (\pi - \theta_0) \cos \theta + \sin \theta_0 \sin \theta \cos \phi. \quad (9)$$

The variations in scattering angle due to changes in VZA and RAZ for different SZAs are demonstrated in Figure 3. As indicated by the number of samples of different scattering angles shown in Figure 4a, the majority of the measurements were made from backward scattering directions with φ ranging from 110° to 160°. To further understand the ADM as shown in Figure 1, the measurements are sorted into "forward" and "backward" groups with corresponding scattering angles
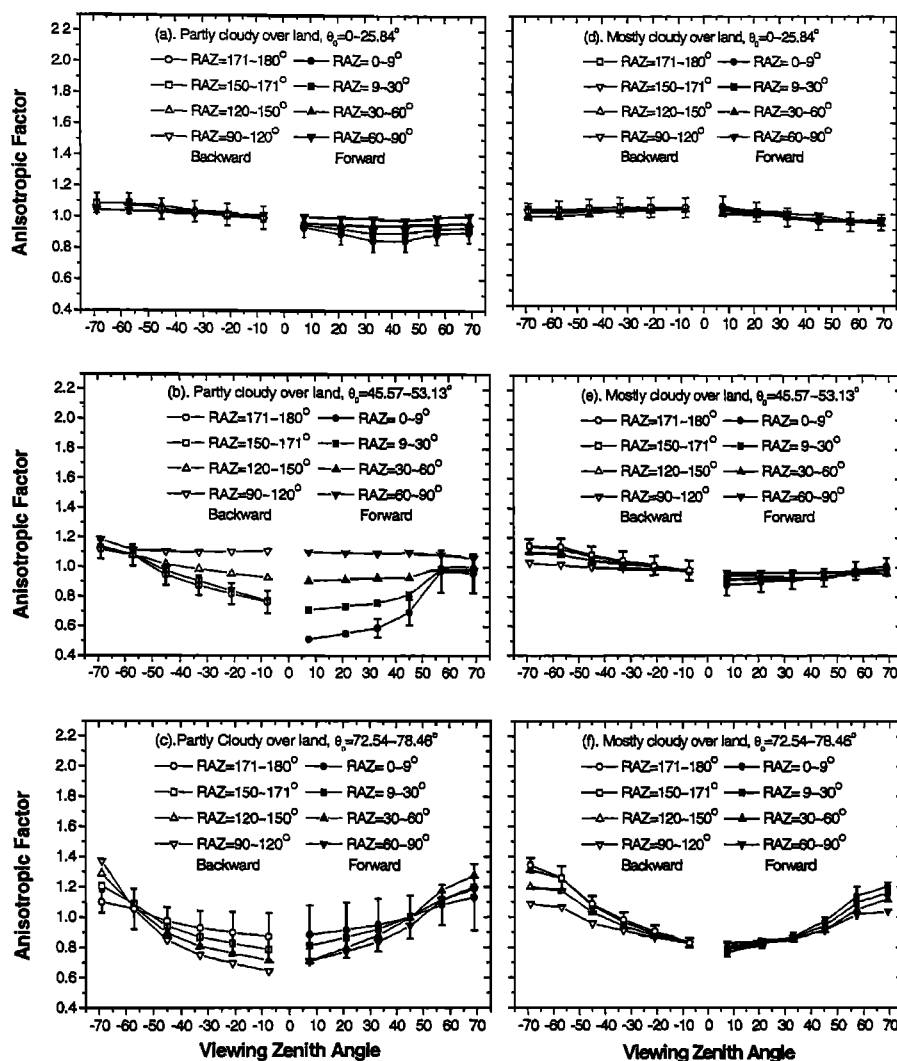
Figure 7. Anisotropic factor at 360 nm derived from Meteor-3 TOMS for partly cloudy and mostly cloudy over land scenes. Note that positive (negative) viewing zenith angles represent forward (backward) directions. The standard deviations are shown as error bars.

marked in Figures 4b and 4c, respectively. The corresponding solar zenith angle is smaller than 45.57°. It is seen that the scattering angles of light received by satellite in backward direction ranges from 110° to 180°, with the majority being around 150°, whereas in forward direction, the corresponding scattering angle roughly varies from 70° to 160°, with a mean around 115°. Therefore radiance scattered in backward directions is generally larger than that in forward directions.

These features can be simulated with a full-fledged Disort-based radiative transfer model for a pure Rayleigh scattering atmosphere bounded by a black surface, i.e., a surface albedo of 0.0. The model results are shown in Figure 5. It follows that the simulated anistropic factor also shows larger values and a more rapid increase with VZA in backward direction (RAZ = 171–180°) than in the forward one. Moreover, the angular dependence is affected significantly by the optical depth of Rayleigh scattering (τ_α). As τ_α increases, the reflection of UV radiation becomes increasingly isotropic.

The standard deviation of anistropic factor is calculated as well, shown in Figure 1 as error bars only for RAZ of 0° ~ 9° and RAZ of 171° ~ 180° for clarity. It is clear that the standard

deviation under clear-sky conditions is relatively small. There is a tendency that it increases with increasing SZA and VZA, due to the few number of samples available at larger SZA and VZA.

3.2. Overcast

Figure 6 presents the ADM derived from TOMS observations at 360 nm under overcast conditions, in comparison with a model-calculated ADM for an atmosphere containing a plane parallel cloud of an optical depth 70. Relative to the ADM for clear over ocean and clear over land scenes, the dependence of ADM for overcast cloud on SZA, RAZ, and VZA is considerably weaker, indicating much less anisotropic reflection by clouds. Multiple scattering by cloud droplets helps smooth out partly the angular dependence. Moreover, the ADM tends to decrease rather than to increase with increasing VZA for small SZAs (Figure 6a, 6d). This can be explained qualitatively by the phase function of cloud droplets as shown in Figure 2. The phase function of water clouds has a sharp peak in the forward scattering direction $(\varphi = 0°)$ and weak peaks in the backward scattering direction $(\varphi = 140°,$
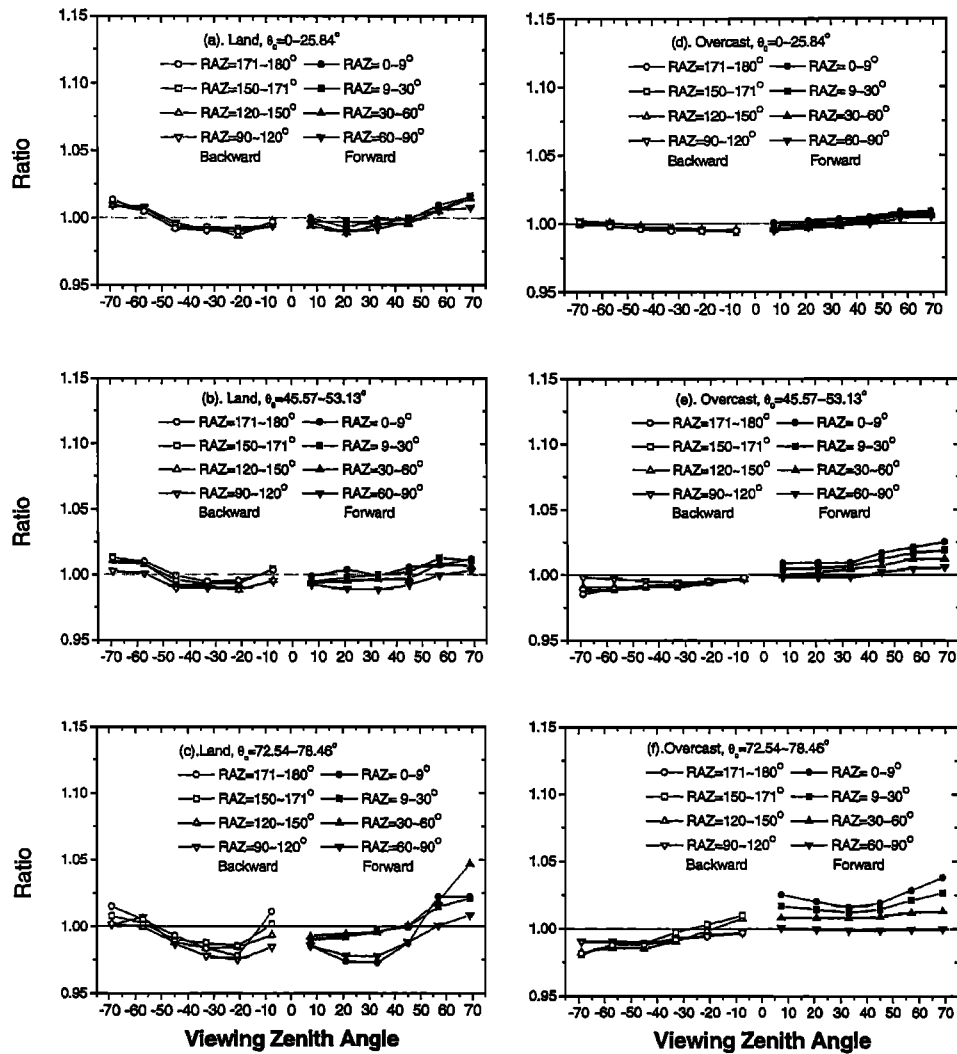
Figure 8. Ratio of the anisotropic factor at 360 nm to that at 340 nm for (a, b, c) clear over land and (d, e, f) overcast scenes.

180°) and a dip in the sideward scattering direction. In comparison with the Rayleigh scattering, the magnitude of variation in the phase function of clouds with varying scattering angle is much stronger. For a small SZA the scattering direction changes from backward to sideward direction as VZA increases, which is accompanied by a slight decrease in the strength of scattering as is shown in Figure 2 and in Figures 6a and 6d. However, for a very large SZA the scattering geometry changes from sideward or backward to forward direction as VZA increases. This results in an evident increase of an anisotropic factor with the increasing VZA (compare Figure 6), as is seen in Figures 6c and 6f. The comparison between the observed and the modeled ADM shows close resemblance for all the ranges of SZA under study. Note that the overcast ADM for UV radiation is somewhat different from that for total solar [*Suttles et al.*, 1988] and visible [*Chang et al.*, 2000] radiation. For the latter two, ADMs at a large SZA show significantly stronger reflection in the forward scattering directions, rather than a more symmetric distribution as is shown in Figure 6. The discrepancy originates from different amounts of contribution by Rayleigh scattering. For total and visible solar radiation, Rayleigh scattering above a cloud top plays a negligible role in comparison to the reflection by the cloud.

Under overcast conditions, the standard deviations of the anisotropic factor becomes considerably smaller (see Figure 6), in comparison with those for clear scenes, although the number of samples is considerably less for overcast scenes. This indicates that reflection of UV radiation from the cloud top is more uniform than that from a clear atmosphere-surface system.

3.3. Partly Cloudy and Mostly Cloudy Scenes

Figure 7 presents the ADMs derived from TOMS observations at 360 nm for partly cloudy and mostly cloudy scenes, which are common scenes in TOMS measurements. It is seen that the magnitude of anistropy for partly and mostly cloudy scenes falls into between the ADM for clear scenes and that for overcast scenes. The variations of the ADM for partly and mostly cloudy scenes with both VZA and RZA are weaker than those for clear scenes but stronger than those for overcast scenes. The ADM for mostly cloudy scenes is less variable than that for partly cloudy scenes. As discussed earlier, Rayleigh scattering is a dominant factor dictating UV ADM under clear-sky conditions, while multiple scattering by clouds smooth out partly the angular variation of backscattered UV radiation under overcast sky. It is thus conceivable to observe the mod-
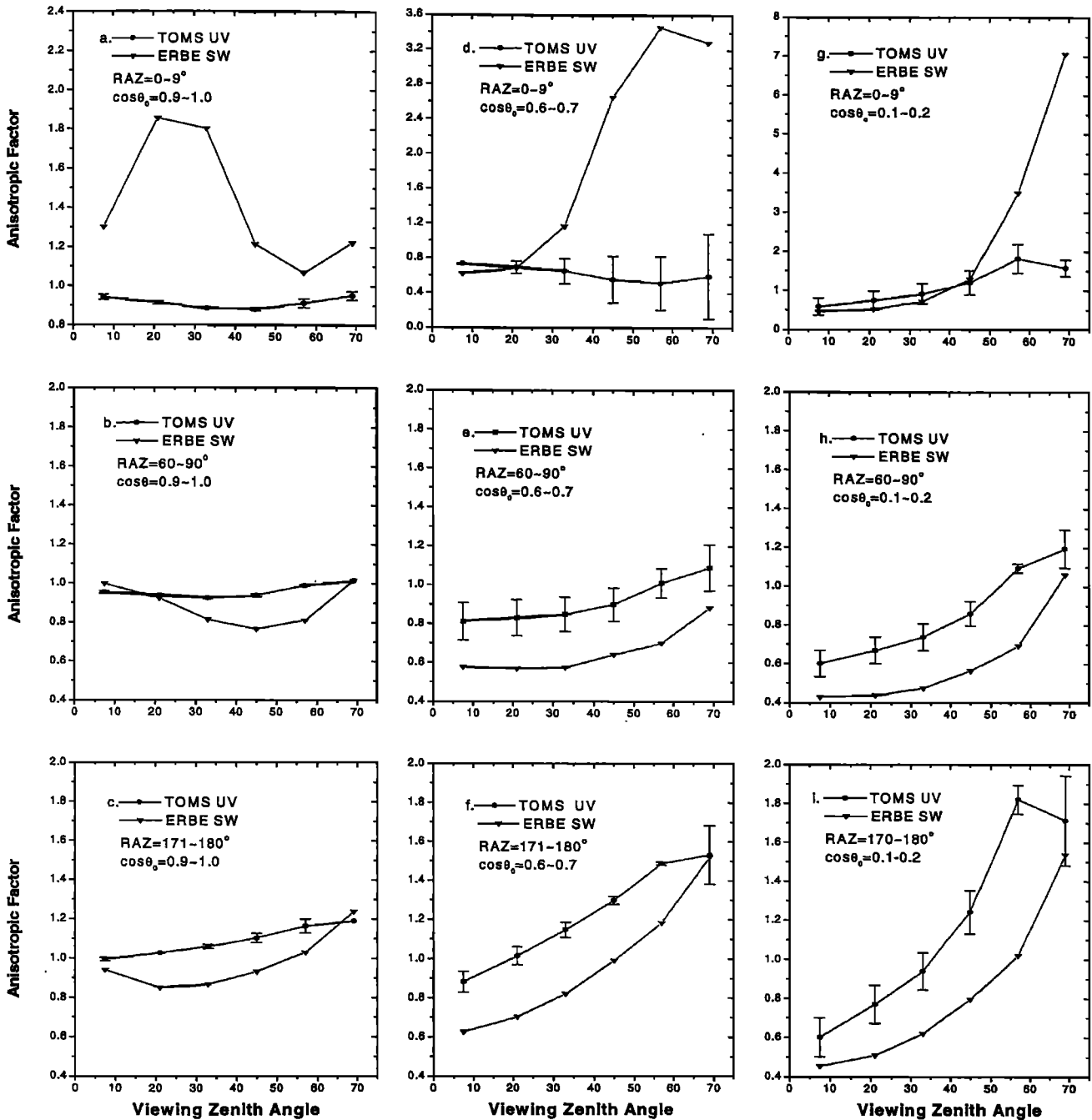
Figure 9. Comparisons between the UV ADM derived from TOMS at 360 nm and the ERBE SW ADM for clear over ocean conditions for different ranges of relative azimuth (RAZ) and cosine of solar zenith ($\cos\theta_0$).

erate anisotropic reflection of backscattered UV radiation for partly and mostly cloudy scenes. Note that the ADM for partly cloudy scenes suffers from the largest uncertainty implied by the largest standard deviation (compare Figure 7). Since the number of samples for this scene type is close to that for clear over land scenes, the largest standard deviation is essentially caused by the nonuniformity of partly cloudy scenes. In comparison, the standard deviation is reduced for mostly cloudy scenes, even though the number of samples is considerably few.

3.4. Variation of ADM With Wavelength

It is known that an ADM depends not only on the scene type but also on the spectral band [*Pinty and Verstraete*, 1992]. To investigate differences among ADMs at different wavelengths, the ratio of ADM at 380 nm to that at 360 nm, as well as 360–340 nm, are computed. Shown in the left-hand and in the right-hand panels of Figure 8 are the ratios of ADM at 360–340 nm for clear land and overcast scenes, respectively. It is seen that the anisotropic factors at 360 nm are very close to those at
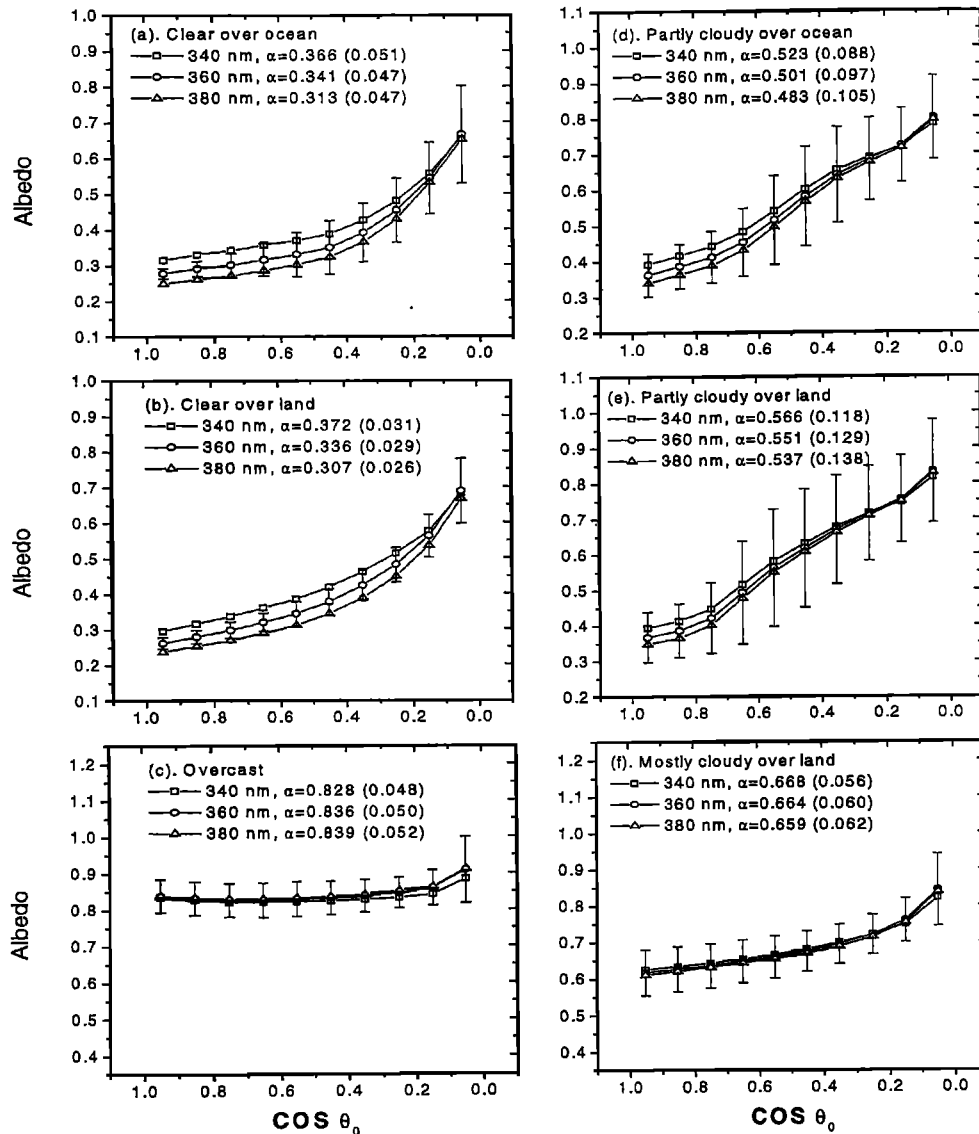
Figure 10. Variations of TOA UV albedos with the cosine of SZA and wavelength derived from TOMS reflectance measurements using the TOMS UV ADM for (a) clear over land, (b) clear over ocean, (c) overcast, (d) partly cloudy over ocean, (e) partly cloudy over land, and (f) mostly cloudy over land scenes. The mean albedo (α) and standard deviation (values in parentheses) are also given.

340 nm for low SZAs. For large SZAs the difference increases somewhat (compare Figures 8c and 8f), but the ratio still varies to within 5%. Similar results are obtained for the ratio between 380 and 360 nm and for both ratios under partly cloudy and mostly cloudy conditions. It is thus concluded that the ADM for 340, 360, and 380 nm may be used without distinction.

On the other hand, however, an ADM developed for a very different spectral region may differ considerably from the UV ADM such as the ERBE ADM for total solar radiation [*Suttles et al.*, 1988]. The latter is the most comprehensive and complete broadband bidirectional model available to date and is thus often treated as the benchmark of ADM. To illustrate the difference between these two sets of ADM, comparisons were made between the ERBE SW and the TOMS UV anisotropic factors for clear ocean scenes (Figure 9). Very large discrepancies are observed in the forward direction (RAZ = 0° ∼ 9°) for all intervals of SZAs where the magnitude of the ERBE ADM is larger than the UV one by several factors. In the

forward scattering direction, total solar radiation reflected by the ocean-atmosphere system is dominated by the specular reflection of the ocean surface, which is extremely anisotropic. For UV radiation, however, the contribution of specular reflection is much reduced because of the enhanced Rayleigh scattering. In sideward and/or backward directions the difference in the anisotropic factors for total and UV radiation becomes much smaller but still quite significant and has opposite signs. It should be mentioned that the ADM for clear over ocean shows the largest discrepancy between the ERBE SW and the TOMS UV ADM. For clear land and overcast scenes, their differences are considerably smaller.

3.5. Derivation of TOA Albedo

A major application for the development of ADM is to derive TOA albedo from reflectance measurements. Figure 10 illustrates the variation of the derived TOA albedos at different UV wavelengths with solar zenith angle. It follows that
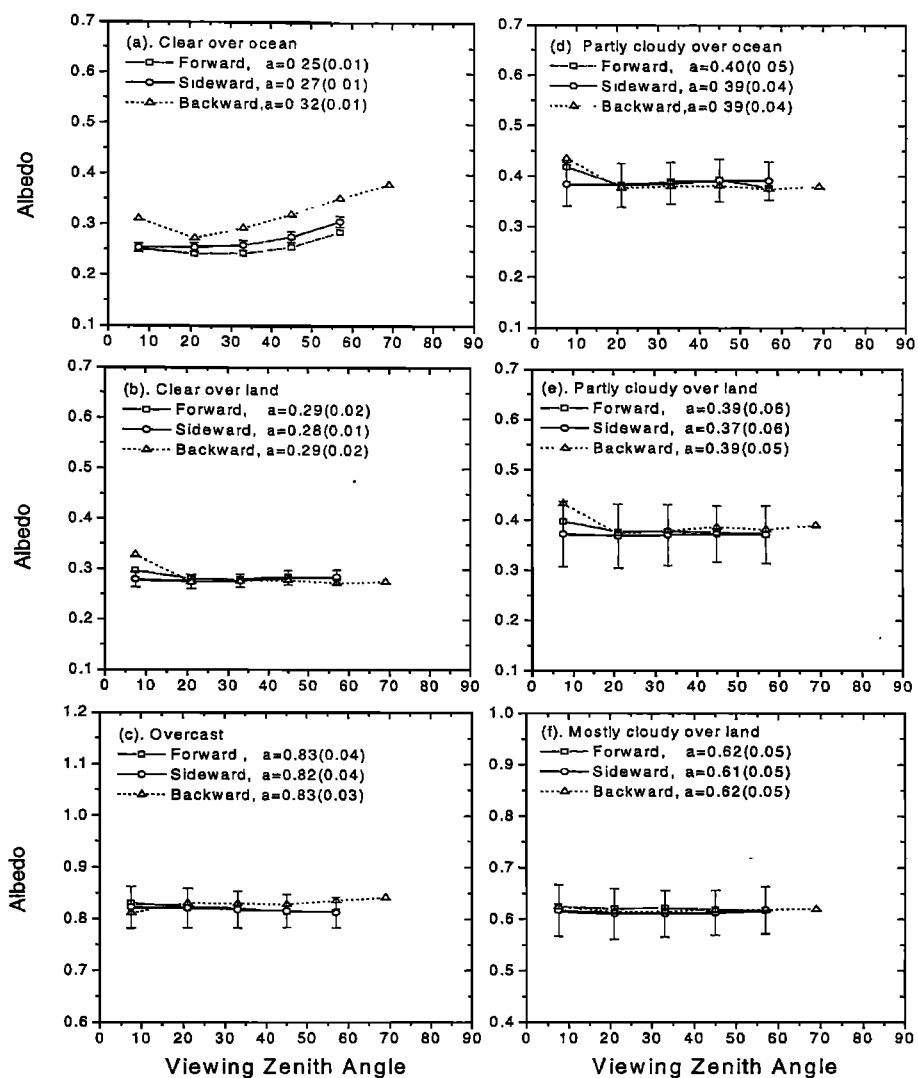
Figure 11. Variations of the TOA UV albedos with the VZA and RZA derived from Nimbus-7/TOMS reflectance measurements using the TOMS UV ADM for (a) clear over land, (b) clear over ocean, (c) overcast, (d) partly cloudy over ocean, (e) partly cloudy over land, and (f) mostly cloudy over land scenes for SZA ranging from 25.84° to 36.87°. The mean albedos (α) and standard deviations (values in parentheses) are also given.

TOA albedo increases with decreasing wavelength, due to the increasing effect of Rayleigh scattering under clear-sky conditions. The mean albedo, as weighted by the number of samples at each of SZA bins, is almost identical for clear land and clear ocean scenes, attesting the negligible effects of the underlying surface. Their mean values averaged over all SZAs (weighted by the number of samples in the corresponding SZA bins) are equal to 0.34 ± 0.03 at 360 nm. It decreases with increasing wavelength: approximately 0.37 ± 0.03, 0.34 ± 0.03, and 0.31 ± 0.03, respectively, for 340, 360, and 380 nm. There is an about 10% difference between the TOA albedos at two neighboring wavelengths. Under overcast conditions, however, TOA albedo only increase with the SZA slightly, and the mean albedo is about 0.83 ± 0.05, similar at all three wavelengths. This is because cloud scattering is independent of wavelength in the UV region [*Stamnes*, 1991], which dominates over the effect of Rayleigh scattering under overcast conditions. For partly cloudy and mostly cloudy over land scenes, the TOA albedo and its variation with wavelength are moderate, relative

to clear and overcast scenes. The mean TOA albedos are 0.57 ± 0.12, 0.55 ± 0.13, and 0.54 ± 0.13, respectively, at 340, 360, and 380 nm for partly cloudy scenes over land and 0.67 ± 0.06, 0.66 ± 0.06, and 0.66 ± 0.06 for mostly cloudy over land scenes. The large standard deviations and changes with SZA are again caused by the nonuniform scenes.

Note that albedos derived from reflectance measurements made from different viewing directions would be identical if perfect ADMs are employed [*Suttles and Wielicki*, 1992]. Given the sampling errors, the albedos may fluctuate within the statistical uncertainties. To evaluate the performance of the TOMS ADM, TOA albedos are computed from reflectance measurements at 360 nm made by Nimbus 7/TOMS from January 1990 to December 1991 in different viewing directions. Figure 11 shows the variation of the albedos over six scene types with the VZA in three RAZ ranges: 0° ~ 60°, 60° ~ 120° and 120° ~ 180°, corresponding, respectively, to forward, sideward, and backward directions. It is seen that the resulting TOA albedos are nearly independent of the VZA for all scene
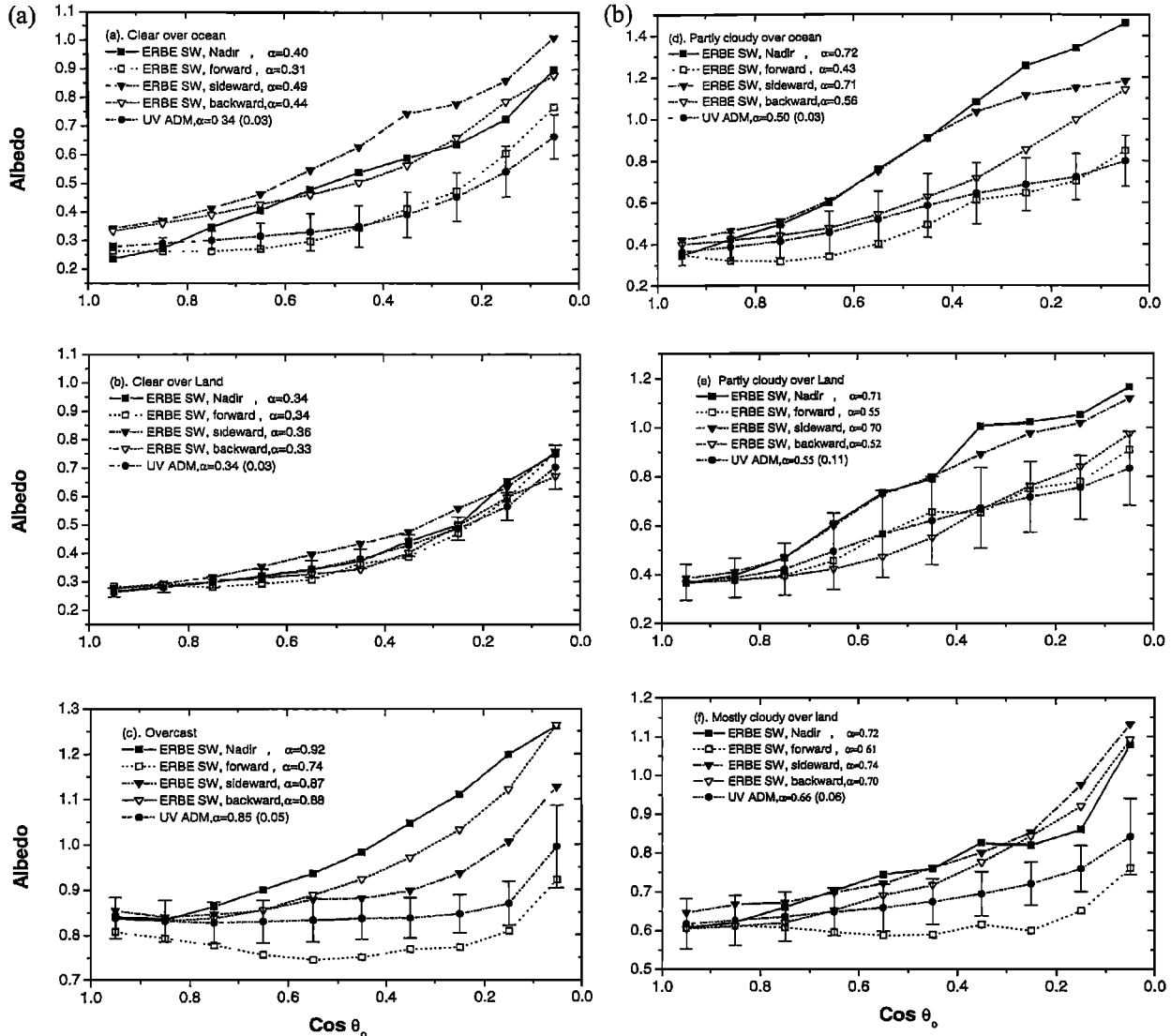
Figure 12. Same as Figure 10 but using ERBE SW ADM.

types except for clear over ocean. The magnitudes of the variations fall basically within the statistical uncertainties of the samples. For clear over ocean, the derived albedos show a slight increase with increasing VZA and have relatively large values at backward direction. Their mean values are 0.25 ± 0.01, 0.27 ± 0.01, and 0.32 ± 0.02, respectively, for forward, sideward, and backward direction. A statistically significant VZA dependence was also found for the ERBE ADM applied to clear ocean scenes [*Suttles and Wielicki*, 1992; *Li*, 1996].

However, when using the ERBE ADM, large discrepancies exist among the albedos estimated from reflectance measurements made from different viewing directions. Figure 12 presents a comparison of TOA albedos at 360 nm derived by applying the ERBE ADM to UV reflectance observed from different directions for overcast, clear over land, clear over ocean scenes, partly cloudy over ocean, partly cloudy over land, and mostly cloudy over land. The same albedos but derived using the corresponding TOMS UV ADM are also shown as benchmark values. The deviation is shown to be quite substantial and generally amplified with increasing SZA. The mean directional albedos as weighted by the number of samples are marked on each plot. For clear ocean scenes, the mean albedos

derived with the ERBE ADM differ from those with the TOMS UV ADM by 21, −6, 48, and 33% (positive values represent overestimation), respectively, for observations made at the nadir, in the forward, sideward, and backward directions. However, for clear land scenes, the albedos derived with the ERBE SW ADM are much more close to those with the TOMS UV ADM. The discrepancies between them are less than 9%. For overcast scenes, the absolute differences are still significant, but relative differences are rather small. The largest overestimation occurred at the nadir view for which the absolute and relative differences in the mean TOA albedo amount to 0.07 and 8.2%, respectively. The overestimation can lead to some TOA albedos larger than unity. In the forward direction, use of the ERBE ADM results in underestimation of TOA albedo by 13%.

It is clear from the above discussion that the ADM for UV radiation is quite different from that for the total solar radiation. The differences between TOA UV albedos derived with the two different sets of ADM depend on Sun-target-sensor geometry as well as on scene type, both of which vary on a global scale. To gain an insight into the spatial variation of the differences, we applied the ERBE SW ADM and TOMS UV
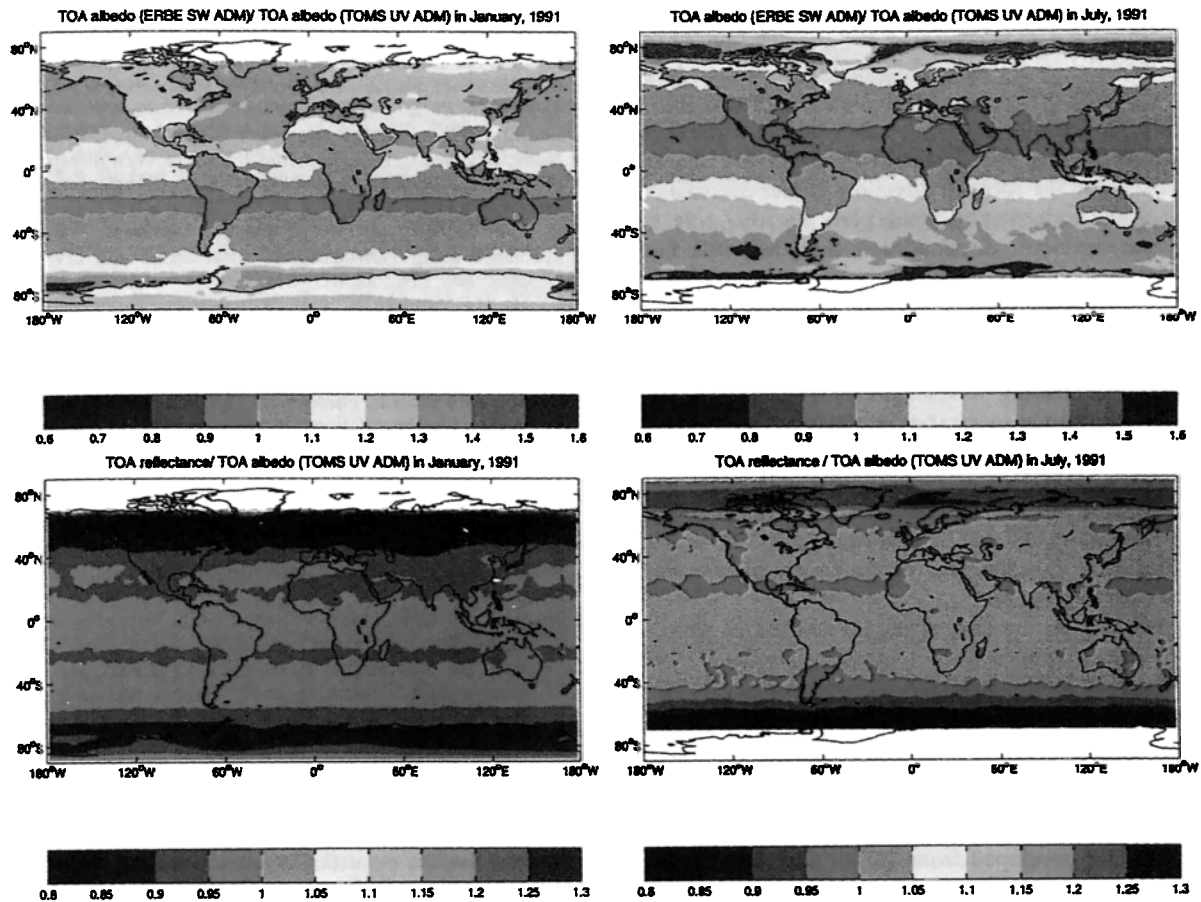
TOA albedo (ERBE SW ADM)/ TOA albedo (TOMS UV ADM) in January, 1991

TOA albedo (ERBE SW ADM)/ TOA albedo (TOMS UV ADM) in July, 1991

TOA reflectance/ TOA albedo (TOMS UV ADM) in January, 1991

TOA reflectance / TOA albedo (TOMS UV ADM) in July, 1991

Plate 1. Global distribution of the ratio of monthly mean TOA albedos converted from Nimbus-7/TOMS measurements using the ERBE SW ADM to that using TOMS UV ADM in January and July 1991 (top two panels). The bottom two panels show the ratio of the UV reflectance as measured by Nimbus 7/TOMS and the corresponding UV albedos derived using the TOMS UV ADM for the same periods.

ADM to calculate global monthly mean TOA UV albedos from independent reflectance measurements made by Nimbus 7/TOMS. The top panels of Plate 1 show the ratios of the resulting TOA albedos at 360 nm derived with the two different sets of ADM in January and July 1991. It is seen that the ratio has an apparent dependence on latitude, or more precisely, on SZA. Good agreements always occur in the summer hemisphere with a minimum difference occurring for overhead Sun. In winter hemisphere, overestimation exceeds 20% over land and 30% over oceans. At high latitudes the overestimation may reach up to 30–50%. Fundamental differences in the radiative transfer of solar and UV radiation is the major underlying reason for the different behaviors of ADM. In the UV spectral region the atmosphere is a much better "diffuser" than it is for total solar radiation. On the other hand, the differences revealed here may result partly from the use of inconsistent scene identification. As stated earlier, the ERBE ADM was designed for application with scene types classified by the MLE, while in this study, they were applied to scenes discriminated using simple thresholds. Any inconsistency in scene classification affects the performance of ERBE ADMs.

Likewise, significant errors are also incurred if isotropic reflection is assumed for the UV radiation reflected by the Earth-atmosphere system; i.e., assuming that reflectance is equal to albedo. The bottom panels in Plate 1 show the ratio of measured TOA reflectance to TOA albedo converted with the

UV ADM in both January and July. It follows that the isotropic assumption generally underestimates TOA albedos for illumination and observation conditions encountered by NIMBUS 7 in January. The amount of underestimation is less than 5% for most lower and middle-latitude regions. While up to 5% overestimation appears for most lower and middle-latitude regions in July, nevertheless, about 20% underestimation occurs at high latitudes in both January and July. These magnitudes of underestimation are in accordance with the simulation results of a radiative transfer model by *Krotkov et al.* [1999].

4. Conclusions

An angular dependence model (ADM) is needed for converting a satellite-measured radiance or reflectance to irradiance or albedo to account for the variation of the sensed target with the Sun-target-satellite geometry. While ADM has been studied rather comprehensively for total and visible solar radiation, no investigation is reported on UV ADM, at least to the knowledge of the authors. As a result, ad hoc assumptions are often resorted to concerning the angular variation of UV radiation for remote sensing surface UV fluxes [*Eck et al.*, 1995; *Wang et al.*, 1999].

In view of this limitation, two and half years of TOMS satellite measurements collected by Meteor 3/TOMS were employed to study the angular behavior of UV radiation. A set of

complete ADM, similar to that for SW radiation used in the ERBE, were developed at the wavelengths of 340, 360, and 380 nm. It is found that the anisotropy of UV reflection by the Earth-atmosphere system is predominately affected by Rayleigh scattering under clear-sky conditions. As a result, the anisotropic factors in the backward direction are generally larger than that in the forward direction. Under overcast conditions, multiple scattering by clouds plays a leading role, rendering a near symmetric distribution in the anisotropic factor between forward and backward directions.

The dependence of ADM on wavelength was also investigated. There are little differences among the ADM at 340, 360, and 380 nm. TOA albedos computed with the developed ADM increase with decreasing wavelength under clear-sky conditions, due to the strong spectral dependence of Rayleigh scattering. The overall mean albedos for clear ocean and land are equal to 0.37 ± 0.03, 0.34 ± 0.03, and 0.31 ± 0.03, respectively, at 340, 360, and 380 nm, whereas the albedos for overcast scenes are almost identical at these wavelengths (0.83 ± 0.05), since scattering by clouds is nearly independent of wavelength in the UV spectral region.

As an assessment of performance, the UV ADM were applied to an independent data set obtained by Nimbus 7/TOMS. The variations of the derived TOA albedos with the VZA for different RZA ranges and different scene types are examined. The results reveal that the albedos are essentially invariant with the viewing geometry. The mean values derived for three different RZA ranges agree to within the statistical uncertainties.

The UV ADM developed from TOMS data are also compared to those for ERBE total solar radiation. There exist large differences between the two sets of ADM, especially for overhead Sun and large viewing zenith angles. Because of the discrepancy in ADM, use of the ERBE ADM to TOMS measured reflectance may introduce significant errors. For example, for clear ocean scenes, the estimation errors are equal to 21, 6, 48, and 33%, respectively, for observations made at nadir, in forward, sideward, and backward directions. For clear land and overcast scenes, however, the discrepancies are reduced considerably to less than 13%. Part of the discrepancies originates from the use of different scene identification schemes. Likewise, the assumption of isotropic reflection for UV radiation also leads to significant errors in the estimation of TOA UV albedo but not so large as using the ERBE ADM. The geographic variation of the uncertainties in generating TOA UV albedos by the two assumptions are also investigated using TOMS data collected by Nimbus 7. The errors are usually small in the summer hemisphere and increases with latitude.

References

Anderson, G. P., S. A. Clough, F. X. Kneizys, J. H. Chetwynd, and E. P. Shettle, AFGL Atmospheric Constituent Profiles (0–120 km), *AFGL Tech. Rep., AFGL-TR-86-0110*, Air Force Geophys. Lab., Air Force Base, Mass., 1986.

Chang, F. L., Z. Li, and A. T. Trishchenko, The dependence of TOA reflectance anisotropy on cloud properties inferred from ScaRaB satellite data, *J. Appl. Meteorol, 39*, 2480–2483, 2000.

Cihlar, J., D. Mandak, and N. Voisin, AVHRR bidirectional reflectance effects and composite, *Remote Sens. Environ., 48*, 77–88, 1994.

Dahlback, A., and K. Stamnes, A new spherical model for computing radiation field available for photolysis and heating at twilight, *Planet. Space. Sci., 39*, 671–683, 1991.

Diner, D. J., G. P. Asner, R. Davies, Y. Knyazikhin, J.-P. Muller, A. W. Nolin, B. Pinty, C. B. Schaaf, and J. Stroeve, New directions in earth observation: Scientific applications of multiangle remote sensing, *Bull. Am. Meteorol. Soc., 80*, 2209–2228, 1999.

Eck, T., P. Barthia, and J. Kerr, Satellite estimation of spectral UVB irradiance using TOMS derived total ozone and UV reflectivity, *Geophys. Res. Lett., 22*, 611–614, 1995.

Fredrick, J. E., and H. E. Snell, Tropospheric influence on solar ultraviolet radiation: The role of clouds, *J. Clim., 3*, 373–381, 1990.

Frederick, J. E., and E. C. Weatherhead, Temporal changes in surface ultraviolet radiation—A study of the Robertson-Berger meter and Dobson data records, *Photochem. Photobiol., 56*, 123–131, 1992.

Gutman, G., On the relationship between monthly mean and maximum-value composite normalized vegetation indices, *Int. J. Remote. Sens., 10*, 1317–1325, 1989.

Gutman, G., Vegetation indices from AVHRR: An update and future prospects, *Remote Sens. Environ., 35*, 121–136, 1991.

Herman, J. R., and E. Celarier, Earth surface reflectivity climatology at 340–380 nm from TOMS data, *J. Geophys. Res., 102*, 28,003–28,012, 1997.

Herman, J. R., et al., Meteor-3 total ozone mapping spectrometer (TOMS) data products user's guide, *NASA Ref. Publ.*, 1996.

Herman, J. R., N. Krotkov, E. Celarier, D. Larko, and G. Labow, Distribution of UV radiation at the Earth's surface from TOMS-measured UV-backscattered radiances, *J. Geophys. Res., 104*, 12,059–12,076, 1999.

Kimes, D. S., B. N. Holben, C. J. Tucker, and W. W., Newcomb, Optimal directional view angles for remote sensing missions, *Int. J. Remote Sens., 5*, 887–908, 1984.

Krotkov, N., J. R. Herman, Z. P. K. Bhartia, Z. Ahmad, and V. Fioletov, Satellite estimation of spectral surface UV irradiance, 2, Effect of horizontally homogeneous clouds and snow, *J. Geophys. Res.*, in press, 1999.

Li, Z., On the angular correction of satellite radiation measurements: The performance of ERBE angular dependence model in the Arctic, *Theor. Appl. Climatol., 54*, 235–248, 1996.

Li, Z., and L. Garand, Estimating surface albedo from space: A parameterization for global application, *J. Geophys. Res., 99*, 8335–8350, 1994.

Li, Z., and H. G. Leighton, Narrowband to broadband conversion with spatially autocorrelated reflectance measurements, *J. Appl. Meteorol., 31*, 421–432, 1992.

Li, Z., J. Cihlar, X. Zhang, L. Moreau, and L. Hung, The bidirectional effect in AVHRR measurements over boreal regions, *IEEE Trans. Geosci. Remote Sens., 34*, 1308–1322, 1996.

Li, Z., P. Wang, and J. Cihlar, A simple and efficient method for retrieving surface UV dose rates, *J. Geophys. Res., 105*, 5027–5036, 2000.

Lubin, D., E. H. Jensen, and H. P. Gies, Global surface ultraviolet radiation climatology from TOMS and ERBE data, *J. Geophys. Res., 103*, 26,061–26,091, 1998.

Middleton, E. M., Solar zenith angle effects on vegetation indices in tallgrass prairie, *Remote Sens. Environ., 38*, 45–62, 1991.

Pinty, B., and M. M. Verstraete, On the design and validation of surface bidirectional reflectance and albedo models, *Remote. Sens. Environ., 41*, 151–167, 1992.

Privette, J. L., D. W. Deering, and D. E. Wickland, Report on the Workshop on Multiangular Remote Sensing for Environmental Applications, *NASA Tech. Memo. 113202*, 56 pp., 1997.

Pubu, C., Solar ultraviolet radiation on the Tibetan Plateau: Measurements and modelling, Ph.D. Dissertation, 27 pp., Univ. of Bergen, Norway, 1998.

Stamnes, K., S. C. Tsay, W. J. Wiscombe, and K. Jayaweera, Numerically stable algorithm for Discrete-Ordinate-Method radiative transfer in multiple scattering and emitting media, *Appl. Opt., 27*, 2502–2509, 1988.

Stamnes, K., J. Slusser, M. Bowen, Derivation of total ozone abundance and cloud effects from spectral irradiance measurements, *Appl. Opt., 30*, 4418–4429, 1991.

Stephens, G. L., Radiation profiles in extended water clouds, II, Parameterization schemes, *J. Atmos. Sci., 35*, 2123–2132, 1978.

Stolarski, P., R. Bojkov, L. Bishop, C. Zerefos, J. Staehelin, and J. Zawodny, Measured trends in stratospheric ozone, *Science, 256*, 342, 1992.

Suttles, J. T., and B. A. Wielicki, Top-of-the-atmosphere radiative fluxes: Validation of ERBE scanner inversion algorithm using Nimbus-7 ERB data, *J. Appl. Meteorol., 31*, 784–796, 1992.

Suttles, J. T., R. N. Green, P. Minnis, G. L. Smith., W. F. Staylor, B. A. Wielicki, I. J. Walker, D. F., Young, V. R. Taylor, and L. L. Stowe, Angular radiation models for Earth-atmosphere system, vol. I, Shortwave radiation, *NASA Ref. Publ., 1184*, 144 pp., 1988.

Tsay, S. C., K. Stamnes, and K. Jayaweera, Radiative transfer in planetary atmospheres: Development and verification of a unified model, *J. Quant. Spectrosc. Radiat. Transfer, 43*, 133–148, 1990.

Wang, P., Z. Li, and D. Wardle, Validation of UV-B inversion algorithm using satellite and surface measurements, *J. Geophy. Res., 105*, 5037–5048, 2000.

Weihs, P., and R. Webb, Accuracy of spectral UV model calculations, 1, Consideration uncertainties in input parameters, *J. Geophys. Res., 102*, 1541–1550, 1997.

Wu, A., Z. Li, and J. Cihlar, Effects of land cover type and greenness on advanced very high resolution radiometer bidirectional reflectance: Analysis and removal, *J. Geophys. Res., 100*, 9179–919, 1995.

Z. Li and C. Pubu, Canada Centre for Remote Sensing, 588 Booth Street, Ottawa, Ontario, Canada, K1A 0Y7. (li@ccrs.nrcan.gc.ca)